Chirality and magnetic quadrupole order in $Pb(TiO)Cu_4(PO_4)_4$ probed by interference scattering in resonant x-ray diffraction

R. Misawa,[1] H. Ueda,[2] K. Kimura,[1] Y. Tanaka,[3] and T. Kimura[1]
[1]*Department of Advanced Materials Science, University of Tokyo, Kashiwa, Chiba 277-8561, Japan*
[2]*Paul Scherrer Institute, Forschungsstrasse 111, 5232 Villigen, Switzerland*
[3]*RIKEN SPring-8 Center, Sayo, Hyogo 679-5148, Japan*

(Received 19 March 2021; revised 20 April 2021; accepted 23 April 2021; published 10 May 2021)

Circular dichroism observed by resonant x-ray diffraction at the Cu L_3 edge was investigated in a chiral antiferromagnet, $Pb(TiO)Cu_4(PO_4)_4$, which shows magnetic quadrupole order ($T_N = 7$ K). At temperatures above T_N, space-group-forbidden reflection 100 is observed due to the anisotropic tensor of susceptibility (ATS) scattering. With decreasing temperature, the reflection intensity shows substantial circular dichroism below T_N. We found one-to-one correspondence between the sign of the circular dichroism and that of the sample's crystallographic chirality. In addition, the reflection intensity depends on the product of poling magnetic and electric fields. The circular dichroism observed in this study is interpreted as the interference between the ATS and the magnetic scatterings. This finding shows that the interference scattering probes both the chirality and the order parameter of the magnetic quadrupole order in this chiral antiferromagnet.

DOI: 10.1103/PhysRevB.103.174409

I. INTRODUCTION

The concept of multipoles, which characterizes spatial distributions of scalar and vector objects by their angular dependence, is of great benefit to understanding physical phenomena in various quantum materials. Multipoles have long been of interest due to their spontaneous ordering in d and f electron systems, which often dominates their electronic properties [1]. Though the multipole has been mainly discussed within single species at a single site [2], this concept is nowadays extended to clusters consisting of several atomic sites in crystalline solids [3,4]. When multipole moments of adjacent clusters in a crystal are arranged in a uniform (staggered) manner, such a state can be regarded as ferroic (antiferroic) order of cluster multipoles. This cluster multipole moment practically functions as a macroscopic order parameter and gives rise to physical phenomena characterized by the symmetry of the multipole. Among various multipoles, magnetic quadrupoles, which are second-rank magnetic multipoles, are one of the most fundamental parity- and time-odd multipoles breaking both space-inversion and time-reversal symmetries. Recently, magnetic quadrupoles are attracting growing interest in the study of cross-coupled physical phenomena such as the linear magnetoelectric (ME) effect, nonreciprocal linear dichroism, the Edelstein effect, and the magnetopiezoelectric effect [5–8]. (Anti)ferroic magnetic quadrupole order has been reported in several magnetic materials including $A(TiO)Cu_4(PO_4)_4$ (A = Ba, Sr, and Pb) [5]. Especially, $Pb(TiO)Cu_4(PO_4)_4$ was found to exhibit ferroic order of magnetic quadrupole moments and a resulting linear ME effect.

$Pb(TiO)Cu_4(PO_4)_4$ crystallizes in a chiral tetragonal structure (space group: $P42_12$, no. 90) which is characterized by a staggered array of upward and downward Cu_4O_{12} square cupola clusters in the (001) plane (see Fig. 1). This compound exhibits antiferromagnetic (AFM) order at $T_N = 7$ K. The magnetic point group in the AFM phase is $4'22'$, which breaks both space-inversion and time-reversal symmetries, and thus allows for a linear ME effect [5]. The spin arrangement in the AFM phase is illustrated in Fig. 1(a) where four Cu spins in each Cu_4O_{12} cluster form a $q_{x^2-y^2}$-type magnetic quadrupole moment. Furthermore, the $q_{x^2-y^2}$ components in the (001) plane on all the Cu_4O_{12} clusters align uniformly, which is depicted by the signs at the centers of the Cu_4O_{12} clusters in Fig. 1(b). This means that ferroic $q_{x^2-y^2}$-type quadrupole order develops in the AFM phase. Recently, remarkable nonreciprocal linear dichroism induced by an optical ME effect, i.e., a linear ME effect for visible light, was reported in the ferroquadrupole ordered phase of $Pb(TiO)Cu_4(PO_4)_4$ [8]. Furthermore, by using the optical ME effect, spatial distributions of a pair of magnetic quadrupoles, i.e., quadrupole domains [$Q+$ and $Q-$ domains depicted in the upper and the lower panels in Fig. 1(b), respectively], were optically visualized.

More recently, it was reported that $Pb(TiO)Cu_4(PO_4)_4$ exhibits an unconventional coupling between crystallographic chirality and magnetism [9]. Since its crystal structure is chiral, both left-handed and right-handed crystals are present as shown in Fig. 1(b) in which the rotation angle of each Cu_4O_{12} square cupola is opposite to each other (see and compare blue and orange circling arrows). Kimura and co-workers reported that the sign of magnetic quadrupole is switched by only a magnetic field without applying an electric field. This electric-field free switching occurs when a magnetic field is applied along the direction slightly tilted from the (001) plane. This is, however, quite unusual since both magnetic and

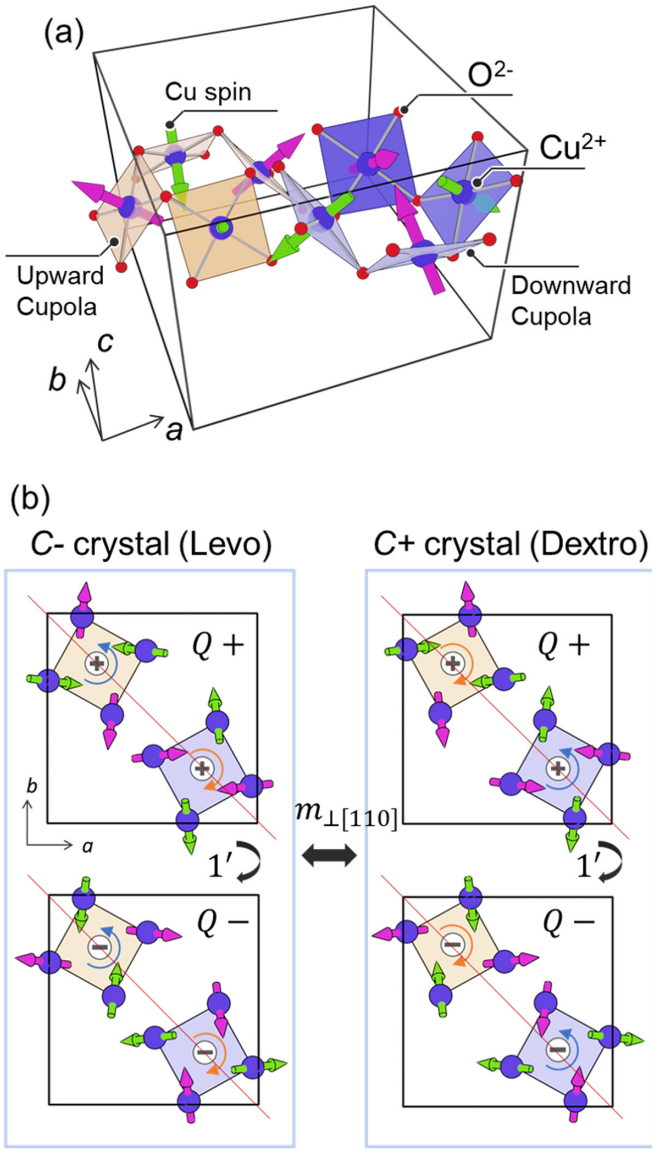

FIG. 1. Crystal and magnetic structures of $Pb(TiO)Cu_4(PO_4)_4$. (a) A three-dimensional view in which Pb, Ti, and P atoms are omitted. A black box denotes a unit cell which contains an upward (orange) and a downward (blue) Cu_4O_{12} square cupolas. Magenta and green arrows represent Cu spins with positive and negative c-axis components, respectively. (b) The c-axis views of levorotatory ($C-$) crystal and dextrorotatory ($C+$) crystal. Only Cu atoms and their spins are depicted. The coordinates of Cu atoms are exaggerated to clarify the difference between $C-$ and $C+$ structures. These two structures are transformed into each other by the mirror operation $m_{\perp[110]}$. The red lines in (b) denote the mirror planes. The upper and the lower panels of (b) illustrate $Q+$ and $Q-$ quadrupole domains, respectively, in each chirality crystal. $Q+$ and $Q-$ domains are mutually converted by the time-reversal operation 1'. The sign (+ or −) in each cupola depicts that of the order parameter in each magnetic quadrupole.

electric fields are needed to switch the sign of the magnetic quadrupole when considering the symmetry of the magnetic quadruple. In addition, the authors found that the sign of the magnetic quadrupole switched by a magnetic field depends on the handedness of crystallographic chirality as well. These unconventional experimental results were interpreted in terms of nonlinear magnetization induced by the combination of chirality and magnetic-field-induced toroidal moment [9–11] or the cross control of magnetic quadrupole and octapole by a magnetic field [9]. This suggests that the introduction of chirality into a ferroquadrupole ordered system causes unconventional magnetic and ME properties. Hence we believe it is worth further pursuing the effect of chirality on magnetic phenomena in $Pb(TiO)Cu_4(PO_4)_4$.

Here we focus on circular dichroism of resonant x-ray diffraction (RXD) [12–14]. RXD is one of the most valuable techniques to unveil ordered states of various types of multipole moments [15–17]. Taking advantage of the polarization state of x rays (circularly polarized x rays), a pair of domains defined by the opposite signs of the order parameter can be resolved. For example, the origin of circular dichroism in Bragg diffraction of heterostructures is discussed in consideration of the chiral array of charge quadrupole moments [18]. In magnetic materials, circular dichroic signals observed in RXD arise through a pure magnetic scattering process, which allows for unambiguous structure determination of spiral spin structures [19]. In addition, interference effects between magnetic and other scatterings [e.g., charge and anisotropic tensor of susceptibility (ATS) scatterings] in RXD can be also responsible for a circular dichroic cross-section of some AFM materials [20,21]. RXD using circularly polarized x rays is also a powerful technique to discern the handedness of crystallographic chirality which is tied with that of the arrangement of electric quadrupole moments [22,23]. In this study, we investigated RXD of the chiral antiferromagnet, $Pb(TiO)Cu_4(PO_4)_4$, by using circularly polarized x rays with the energy near the Cu $L_{2,3}$ edges to examine the order parameters of both the chirality and the magnetic quadrupole.

II. EXPERIMENT

Single crystals of $Pb(TiO)Cu_4(PO_4)_4$ were grown by the slow-cooling method. Figure 2(a) displays magnetic susceptibility and specific heat of some of the grown crystals, which confirms that the crystals undergo an AFM transition at $T_N = 7$ K. The crystallographic chirality of the crystals studied here was checked with white light by means of polarized light microscopy. We defined the crystal chirality $C-$ and $C+$ by a sense of optical rotatory, i.e., levorotatory and dextrorotatory, respectively. Monodomain crystals, either $C+$ or $C-$, were used for RXD measurements. The orientation of the crystals was determined using Laue x-ray photograph. The crystals were cut into thin plates with the widest faces parallel to the (100) plane. The scattering (100) surface of the samples was mechanically polished using diamond slurries with an average particle size down to 0.25 μm.

RXD measurements on these samples were performed using a renewed diffractometer based on the prototype instrument [24] at the beamline 17SU, SPring-8, Japan. In our RXD measurements, circular dichroism on reflection 100 was examined. The photon energy of incident x rays was tuned in the vicinity of the Cu $L_{2,3}$ absorption edges. The degree of the circular polarization of the incident x rays was $|P_2| \geqslant 90\%$ in which P_2 is the Poincaré-Stokes parameter

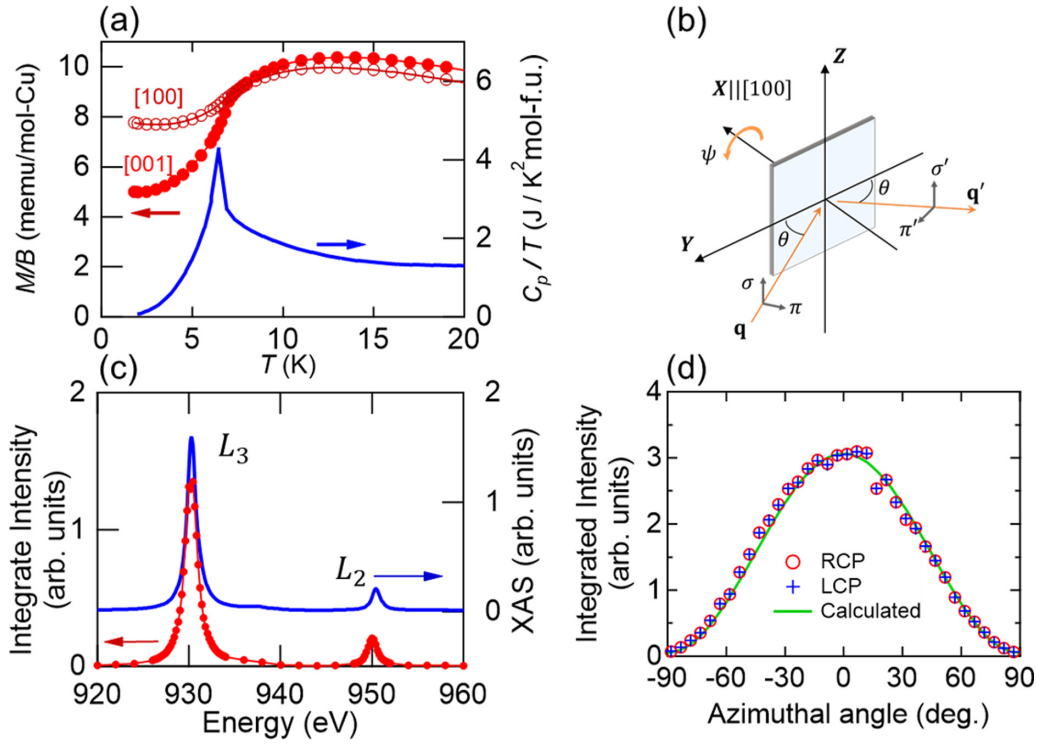

FIG. 2. Characterization of $Pb(TiO)Cu_4(PO_4)_4$. (a) Temperature (T) profiles of magnetization (M) divided by magnetic field (B) of 0.5 T applied along the [100] and [001] directions and specific heat (C_p) divided by T in the absence of B [5]. (b) The scattering geometry. Here, $\mathbf{q}$ and $\mathbf{q}'$ are the propagation vectors of the incident and diffracted x rays, respectively, and θ denotes the Bragg angle. The $\boldsymbol{\sigma}$ and $\boldsymbol{\sigma}'$ components are perpendicular to the scattering plane, and the $\boldsymbol{\pi}$ and $\boldsymbol{\pi}'$ components are parallel to the scattering plane. (c) Photon-energy profiles of x-ray absorption (blue) and forbidden reflection 100 (red) at the azimuthal angle $\psi = 0°$. These data were taken at room temperature using LCP incident x rays. (d) Azimuthal angle dependence of the forbidden reflection 100. These data were taken at room temperature using LCP and RCP incident x rays. The solid line is calculated from the crystal structure by the first-principles calculation, utilizing FDMNES software [28,29].

characterizing the circular polarization of x rays. The polarization state with $P_2 = +1$ corresponds to right-handed circularly polarized (RCP) x rays while that with $P_2 = -1$ means left-handed circularly polarized (LCP) ones [25]. The intensity of diffracted x rays was monitored using a Si-photodiode sensor. A schematic drawing of the experimental setup is shown in Fig. 2(b). The samples were mounted on the diffractometer so that the [100] direction was along the momentum transfer vector ($\boldsymbol{\tau} = \mathbf{q} - \mathbf{q}'$) where $\mathbf{q}$ and $\mathbf{q}'$ are the wave vectors of the incident and scattered x rays, respectively. The rotation of the sample about the momentum transfer vector is defined by the azimuthal angle ψ. The origin $\psi = 0$ was defined when the [001] direction is perpendicular to the scattering plane [parallel to the z axis in Fig. 2(b)].

To examine effects of electric- and magnetic-field poling on RXD at reflection 100, both a magnetic field B and an electric field E were applied along the [010] direction while cooling the sample (ME cooling). The RXD measurements were performed at $\psi = 0$. $B(\approx 0.1\,\mathrm{T})$ was applied by using a pair of samarium-cobalt magnets and $E(|E| \leqslant 2\,\mathrm{MV\,m^{-1}})$ was applied with a voltage source during ME cooling. This procedure stabilizes one of the ferroic Q domains ($Q+$ or $Q-$) [Fig. 1(b)], which has been confirmed by previous ME measurements [5]. To take two-dimensional maps of the diffracted x-ray intensity of reflection 100, the sample position was moved by an XYZ translation stage with 20 μm (25 μm) step in a horizontal (vertical) direction. For the map measurements, the incident x-ray beam was focused into approximately 30 μm (15 μm) horizontally (vertically) by using Kirkpatrick-Baez configuration mirrors.

III. FORMULATION OF RESONANT X-RAY DIFFRACTION

A. General scattering factor

To discuss experimental results, we adopt the general theory of resonant x-ray diffraction from magnetic materials [12,21]. The atomic scattering factor derived in the range of resonant dipole transitions is formulated as follows:

$$f_{\mathrm{atom}} = -(\widehat{\boldsymbol{\varepsilon}'} \cdot \hat{\boldsymbol{\varepsilon}})\left[f_0 + \left(\frac{3}{4\pi q}\right)\left(F^1_{-1} + F^1_{+1}\right)\right] - \left(\frac{3}{4\pi q}\right) i(\widehat{\boldsymbol{\varepsilon}'} \times \hat{\boldsymbol{\varepsilon}}) \cdot \hat{\mathbf{m}}\left(F^1_{-1} - F^1_{+1}\right) + f^{dd}_{\mathrm{Res}}. \quad (1)$$

Here, $\hat{\boldsymbol{\varepsilon}}$ ($\widehat{\boldsymbol{\varepsilon}'}$) denotes the polarization unit vector of the incident (diffracted) x-ray beam, f_0 is the Thomson charge scattering length, and q is the wave number of a photon. F^1_ν and $\hat{\mathbf{m}}$ are the resonant strengths of the dipole transition with a change in magnetic quantum number ν and the unit vector parallel to the magnetic moment, respectively. The first term is the nonmagnetic, including nonresonant f_0 and resonant charge scatterings $F^1_{-1} + F^1_{+1}$, and the second term is the resonant magnetic scattering. For simplification, higher-order

terms of $\hat{\mathbf{m}}$ are ignored. The last term f_{Res}^{dd} is the resonant term from the ground state with an affix "dd" for two dipole transitions and is called as Templeton-Templeton scattering [26] or anisotropic tensor of susceptibility (ATS) scattering [27]. This scattering length is not zero at the absorption edge due to the anisotropic feature of the electronic multipoles of resonant ions with its site symmetry. Including the two polarization vectors, $\hat{\boldsymbol{\varepsilon}}$ and $\widehat{\boldsymbol{\varepsilon}'}$, the last term in Eq. (1) is obtained as

$$f_{\mathrm{Res}}^{dd} = \sum_n \frac{m(E_a - E_n)^2}{\hbar^2}\left[\frac{\langle a|(\widehat{\boldsymbol{\varepsilon}'}\cdot\mathbf{r})|n\rangle\langle n|(\hat{\boldsymbol{\varepsilon}}\cdot\mathbf{r})|a\rangle}{E_a - E_n + \hbar\omega - \frac{i\Gamma_n}{2}}\right] = \widehat{\boldsymbol{\varepsilon}'}\cdot\hat{T}\cdot\hat{\boldsymbol{\varepsilon}}, \tag{2}$$

where $\mathbf{r}$ is the position of the scattered electron, the tensor $\hat{T}$ is a representation of the two polarization vectors for the $E1$-$E1$ transition (two electric dipole transitions) from $|a\rangle$ at the energy of E_a to the intermediate state $|n\rangle$ at the energy of E_n using photon energy of $\hbar\omega$, and Γ_n is the width. From this equation, one can write tensorial scattering factor $\hat{T}$ as a second rank symmetric tensor. This tensorial quantity remains invariant under the symmetry operation of a specific site occupied by the resonant atoms. In $Pb(TiO)Cu_4(PO_4)_4$, the site symmetry of Cu atom is 1 with Wyckoff letter $8g$ [5], and then all the components of $\hat{T}$ are allowed. This ATS scattering term plays an important role in our study.

The unit-cell resonant scattering factor f from a magnetic crystal at the scattering vector $\boldsymbol{\tau}$ is given by taking Fourier transform of Eq. (1),

$$f = -\sum_j e^{i\boldsymbol{\tau}\cdot\mathbf{R}_j}(\widehat{\boldsymbol{\varepsilon}'}\cdot\hat{\boldsymbol{\varepsilon}})\left[f_{0j} + \left(\frac{3}{4\pi q}\right)\left(F_{-1}{}^1 + F_{+1}{}^1\right)\right] - \left(\frac{3}{4\pi q}\right) i\sum_j e^{i\boldsymbol{\tau}\cdot\mathbf{R}_j}(\widehat{\boldsymbol{\varepsilon}'}\times\hat{\boldsymbol{\varepsilon}})\cdot\hat{\mathbf{m}}_j\left(F_{-1}{}^1 - F_{+1}{}^1\right) + \widehat{\boldsymbol{\varepsilon}'}\cdot\left[\sum_j e^{i\boldsymbol{\tau}\cdot\mathbf{R}_j}\hat{R}(\mathbf{g}^j)\hat{T}^1\hat{R}^{-1}(\mathbf{g}^j)\right]\cdot\hat{\boldsymbol{\varepsilon}}. \tag{3}$$

$\mathbf{R}_j$ and $\hat{\mathbf{m}}_j$ represent the position and the unit vector along the local magnetic moment of the atom at site j, respectively. In the last term, $\hat{T}^1$ is the $\hat{T}$ for atom 1 in the unit cell and $\hat{R}(\mathbf{g}^j)$ is the matrix of the symmetry operation $\mathbf{g}^j$ that relates the position of atom j to the position of atom 1. Here, one can define the crystal structure factor, the nonresonant charge scattering $F_c = \sum_j e^{i\boldsymbol{\tau}\cdot\mathbf{R}_j} f_{0j}$, the resonant charge scattering $F_c' + iF_c'' = (3/4\pi q)\sum_j e^{i\boldsymbol{\tau}\cdot\mathbf{R}_j}(F_{-1}{}^1 + F_{+1}{}^1)$, the resonant magnetic scattering $\mathbf{F}_m = -(3/4\pi q)i\sum_j e^{i\boldsymbol{\tau}\cdot\mathbf{R}_j}\hat{\mathbf{m}}_j\ (F_{-1}{}^1 - F_{+1}{}^1)$, and the ATS scattering $\hat{F}_{\mathrm{ATS}} = \sum_j e^{i\boldsymbol{\tau}\cdot\mathbf{R}_j}[\sum_j e^{i\boldsymbol{\tau}\cdot\mathbf{R}_j}\hat{R}(\mathbf{g}^j)\hat{T}^1\hat{R}^{-1}(\mathbf{g}^j)]$.

The photon polarization dependence is given by

$$\widehat{\boldsymbol{\varepsilon}'}\cdot\hat{\boldsymbol{\varepsilon}} = \begin{pmatrix}\boldsymbol{\sigma}'\cdot\boldsymbol{\sigma} & \boldsymbol{\sigma}'\cdot\boldsymbol{\pi}\\ \boldsymbol{\pi}'\cdot\boldsymbol{\sigma} & \boldsymbol{\pi}'\cdot\boldsymbol{\pi}\end{pmatrix} = \begin{pmatrix}1 & 0\\ 0 & \widehat{\mathbf{q}'}\cdot\hat{\mathbf{q}}\end{pmatrix} = \begin{pmatrix}1 & 0\\ 0 & \cos 2\theta\end{pmatrix} \tag{4}$$

and

$$\widehat{\boldsymbol{\varepsilon}'}\times\hat{\boldsymbol{\varepsilon}} = \begin{pmatrix}\boldsymbol{\sigma}'\times\boldsymbol{\sigma} & \boldsymbol{\sigma}'\times\boldsymbol{\pi}\\ \boldsymbol{\pi}'\times\boldsymbol{\sigma} & \boldsymbol{\pi}'\times\boldsymbol{\pi}\end{pmatrix} = \begin{pmatrix}0 & \hat{\mathbf{q}}\\ -\widehat{\mathbf{q}'} & \widehat{\mathbf{q}'}\times\hat{\mathbf{q}}\end{pmatrix}, \tag{5}$$

whose bases are perpendicular ($\boldsymbol{\sigma}$ and $\boldsymbol{\sigma}'$) and parallel ($\boldsymbol{\pi}$ and $\boldsymbol{\pi}'$) to the scattering plane, where orthogonal conditions $\boldsymbol{\sigma}\times\boldsymbol{\pi} = \hat{\mathbf{q}}$ and $\boldsymbol{\sigma}'\times\boldsymbol{\pi}' = \widehat{\mathbf{q}'}$ hold. Here θ is the Bragg angle, and $\hat{\mathbf{q}}$ ($\widehat{\mathbf{q}'}$) is the unit vector parallel to $\mathbf{q}$ ($\mathbf{q}'$). The diffraction geometry is shown in Fig. 2(b). In this geometry, each component is explicitly expressed as

$$\hat{\mathbf{q}} = \begin{pmatrix}\sin\theta\\ -\cos\theta\\ 0\end{pmatrix},\quad \widehat{\mathbf{q}'} = \begin{pmatrix}-\sin\theta\\ -\cos\theta\\ 0\end{pmatrix},\ \boldsymbol{\sigma},\quad \boldsymbol{\sigma}' = \begin{pmatrix}0\\ 0\\ 1\end{pmatrix},$$

$$\boldsymbol{\pi} = \begin{pmatrix}-\cos\theta\\ -\sin\theta\\ 0\end{pmatrix},\quad \boldsymbol{\pi}' = \begin{pmatrix}-\cos\theta\\ \sin\theta\\ 0\end{pmatrix},$$

$$\text{and}\quad \widehat{\mathbf{q}'}\times\hat{\mathbf{q}} = \begin{pmatrix}0\\ 0\\ \sin 2\theta\end{pmatrix}. \tag{6}$$

B. Structure factors of $Pb(TiO)Cu_4(PO_4)_4$

We derive the structure factor at reflection 100 of $Pb(TiO)Cu_4(PO_4)_4$. In the following derivation, we use crystallographic and magnetic structure data reported in Ref. [5]. In a unit cell of its space group $P42_12$, Cu atoms locate at Wyckoff letter g sites with multiplicity 8 [(x, y, z), $(-x, -y, z)$, $(1/2 - y, 1/2 + x, -z)$, $(1/2 + y, 1/2 - x, z)$, $(1/2 - x, 1/2 + y, -z)$), $(1/2 + x, 1/2 - y, -z)$, $(y, x, -z)$, and $(-y, -x, -z)$ where $x = 0.267$, $y = 0.981$, and $z = 0.401$]. For $\boldsymbol{\tau} = (1\,0\,0)$, the Fourier component $\sum_j e^{i\boldsymbol{\tau}\cdot\mathbf{R}_j}$ is zero. Hence, the crystal structure factor for nonresonant and resonant scatterings in the first term in Eq. (3) is zero, meaning that reflection 100 is forbidden.

Meanwhile, in the space group $P42_12$ having twofold spiral axes parallel to [100], the presence of ATS scattering at $\boldsymbol{\tau} = (1\,0\,0)$ is expected under a resonant condition [27]. The form factor for the ATS scattering $\hat{F}_{\mathrm{ATS}}$ is obtained by defining $\hat{T}$ for atom 1 as T_{ij} $(i, j = x, y, z)$ and by calculating $[\sum_j e^{i\boldsymbol{\tau}\cdot\mathbf{R}_j}\hat{R}(\mathbf{g}^j)\hat{T}^1\hat{R}^{-1}(\mathbf{g}^j)]$. $\hat{F}_{\mathrm{ATS}}$ at 100 is calculated by using the three-dimensional basis shown in Fig. 2(b), and is obtained as

$$\hat{F}_{\mathrm{ATS}}(0) = \begin{pmatrix}0 & F_1 & iF_2\\ F_1 & 0 & 0\\ iF_2 & 0 & 0\end{pmatrix},$$

$$\hat{F}_{\mathrm{ATS}}(\psi) = \begin{pmatrix}1 & 0 & 0\\ 0 & \cos\psi & \sin\psi\\ 0 & -\sin\psi & \cos\psi\end{pmatrix}\begin{pmatrix}0 & F_1 & iF_2\\ F_1 & 0 & 0\\ iF_2 & 0 & 0\end{pmatrix}\times\begin{pmatrix}1 & 0 & 0\\ 0 & \cos\psi & -\sin\psi\\ 0 & \sin\psi & \cos\psi\end{pmatrix},$$

$$\widehat{\boldsymbol{\varepsilon}'}\cdot\hat{F}_{\mathrm{ATS}}\cdot\hat{\boldsymbol{\varepsilon}} = \cos\theta(F_1\sin\psi - iF_2\cos\psi)\begin{pmatrix}0 & 1\\ 1 & 0\end{pmatrix}, \tag{7}$$

where F_1 and F_2 are two independent components [$F_1 = 4T_{xy}(\cos 2\pi x + \cos 2\pi y)$, $iF_2 = 4i(T_{zx}\sin 2\pi x - T_{yz}\sin 2\pi y)$ for the atomic coordinate at $(x,\ y,\ z)$]. Here F_1 and F_2 are real numbers. Therefore, the diffraction intensity due to the ATS scattering for any perfect polarization of incident x rays is

$$I_{\mathrm{ATS}} \propto F_2^2\cos^2\psi + F_1^2\sin^2\psi. \tag{8}$$

As shown in Fig. 2(a), $Pb(TiO)Cu_4(PO_4)_4$ exhibits an AFM order below T_N. The magnetic structure reported in Ref. [5] possesses the modulation wave vector $\mathbf{k} = (0, 0, 0)$ and the moment direction on each Cu atom $\{\mathbf{m} = (m_a, m_b, m_c) = [0.469(5), -0.06(7), -0.531(6)]\}$ below T_N (see Fig. 1). Symmetry operations with these parameters give the magnetic structure factor at reflection 100 as a function of ψ,

$$\mathbf{F}_m(0) = \sum_j \hat{\mathbf{m}}_j e^{i\boldsymbol{\tau}\cdot\mathbf{R}_j} = \begin{pmatrix} 0 \\ iF_{mb} \\ F_{mc} \end{pmatrix},$$

$$\mathbf{F}_m(\psi) = \begin{pmatrix} 1 & 0 & 0 \\ 0 & \cos\psi & \sin\psi \\ 0 & -\sin\psi & \cos\psi \end{pmatrix}\begin{pmatrix} 0 \\ iF_{mb} \\ F_{mc} \end{pmatrix}$$

$$= \begin{pmatrix} 0 \\ i\cos\psi F_{mb} + \sin\psi F_{mc} \\ -i\sin\psi F_{mb} + \cos\psi F_{mc} \end{pmatrix}. \tag{9}$$

Here $F_{mb} = 4(\frac{m_b}{|\mathbf{m}|}\sin(2\pi x) - \frac{m_a}{|\mathbf{m}|}\sin(2\pi y))$ and $F_{mc} = 4\frac{m_c}{|\mathbf{m}|}[\cos(2\pi x) + \cos(2\pi y)]$ are real numbers ($|F_{mb}| = 0.02$ and $|F_{mc}| = 2.65$). The sign of $\mathbf{F}_m$ depends on that of the time-reversal domain (= magnetic quadrupole domain). Note that the reversal of the crystallographic chirality, $(C+, C-)$, reverses the sign of F_{mb} but not F_{mc}, which is ascribed to the Dzyaloshinskii-Moriya interaction. This leads to chirality in magnetic structure, i.e., magnetic chirality, too [compare magnetic structures depicted in the left and right panels of Fig. 1(b) and find a mirror relation between them]. Thus, magnetic chirality induced by crystallographic chirality is present in the chiral antiferromagnet, $Pb(TiO)Cu_4(PO_4)_4$.

IV. RESULTS AND DISCUSSION

A. ATS scattering at room temperature

Figure 2(c) shows the integrated intensity of reflection 100 as a function of the photon energy of incident x rays (E_{ph}) in the vicinity of the Cu $L_{2,3}$ absorption edges. The intensity is integrated by an ω scan at each energy point. The data were taken at room temperature ($\gg T_N$) for sample 1 whose details are described in the next subsection. To show the absorption edges, we overlay the corresponding x-ray absorption spectrum (XAS), in which a strong peak and a weak peak appear around the Cu L_3 and L_2 edges, respectively. As mentioned in Sec. III B, there is no signal in the nonresonant condition because reflection 100 is forbidden. Corresponding to the XAS, reflection 100 is strongly enhanced at the L_3 edge, whereas its enhancement at the L_2 edge is smaller. Since these data were taken in the paramagnetic phase, the resonant enhancement of reflection 100 is not ascribed to a magnetic scattering.

To clarify the origin of the resonant enhancement of space-group forbidden reflection 100, we measured the azimuthal angle (ψ) dependence of the reflection at $E_{\mathrm{ph}} = 930$ eV corresponding to the Cu L_3 edge where reflection 100 showed the maximum intensity. In this condition, the Bragg angle θ is $\theta \approx 44.8^\circ$. Figure 2(d) shows the integrated intensity of reflection 100 as a function of ψ. We found that it is independent of the circular polarization of incident x rays and is well fitted to the function $\cos^2\psi$. Introducing $|F_1| \ll |F_2|$ to Eq. (7), the diffraction intensity due to the ATS scattering I_{ATS} becomes nearly proportional to $\cos^2\psi$, which matches up well with the experimental results shown in Fig. 2(d). In addition, Eq. (7) gives that I_{ATS} is independent of the incident polarization state for the completely polarized light. This is also consistent with our experimental results. Thus, it is fair to say that the resonant enhancement of reflection 100 is ascribed to the ATS scattering where $|F_1|$ is negligibly smaller than $|F_2|$. Furthermore, we also confirmed that the observed ψ dependence of the reflection intensity shows good agreement with the result of the first-principles calculation obtained by the simulation software FDMNES [28,29] [green solid line in Fig. 2(d)].

B. Circular dichroism observed below T_N

Next, we examined an effect of magnetic order on the resonant x-ray diffraction at reflection 100. The sample used in this experiment (sample 1) is a dextrorotatory ($C+$) crystal whose photo is shown in Fig. 3(d). Note that the magnetic structure of ferroquadrupole ordered $Pb(TiO)Cu_4(PO_4)_4$ (Fig. 1) is characterized by the modulation wave vector $\mathbf{k} = (0, 0, 0)$ [5]. Thus, the order will affect reflection 100. The following experiment was carried out at $E_{\mathrm{ph}} = 930$ eV. Sample 1 was cooled down to temperatures around T_N. Figures 3(a) and 3(b) show the H-scan profiles of reflection 100 obtained by using circularly polarized incident x rays at 7.8 K ($> T_N$) and 6 K ($< T_N$), respectively. During the cooling process and the measurement, no electric and magnetic fields were applied. The azimuth angle was set to $\psi = 0^\circ$ to maximize the contribution from the ATS scattering. As seen in Fig. 3(a), no circular dichroic signal was observed in the paramagnetic phase. By contrast, the profile in the ferroquadrupole ordered phase clearly shows circular dichroism in which the LCP data are larger than the RCP data [Fig. 3(b)]. Figure 3(c) displays the flipping ratio (FR) defined as a normalized difference of the integrated intensity between the LCP and RCP data, $(I_{\mathrm{LCP}} - I_{\mathrm{RCP}})/(I_{\mathrm{RCP}} + I_{\mathrm{LCP}})$, as a function of temperature, which shows that the circular dichroism appears at T_N and develops with decreasing temperature. This indicates that the magnetic order is responsible for the circular dichroism of reflection 100.

We also investigated spatial distributions of the observed circular dichroism by scanning a focused x-ray beam on the surface of sample 1 [an area surrounded by a red broken box of Fig. 3(d)]. The beam size is described in Sec. II. The results are displayed in Figs. 3(e) and 3(f), which plot two-dimensional maps of FR taken at room temperature ($> T_N$) and 6 K ($< T_N$), respectively. The former map is white in

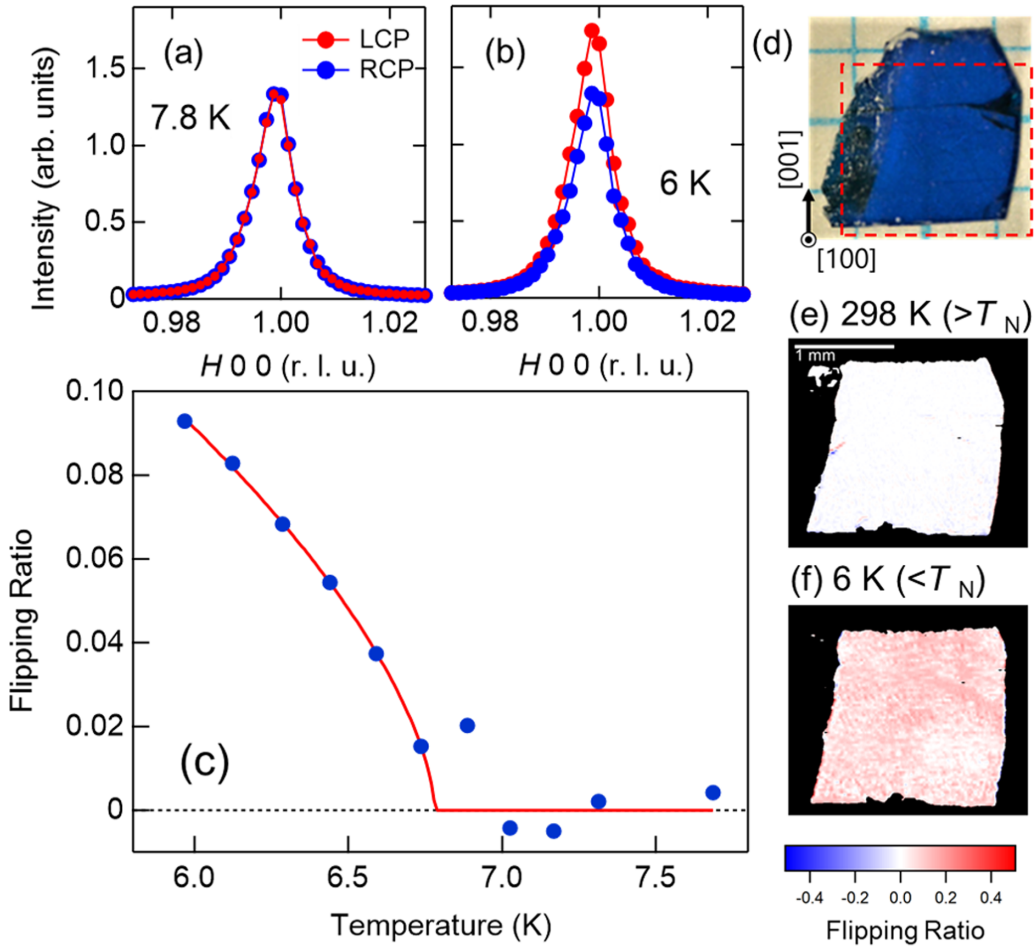

FIG. 3. Circular dichroism of resonant x-ray diffraction below $T_N = 7$ K at $\psi = 0^\circ$ in a dextrorotatory ($C+$) crystal (sample 1). (a), (b) Comparison of the H-scan profiles around 100 obtained with LCP and RCP incident x rays at (a) 7.8 K and (b) 6 K. (c) Temperature dependence of flipping ratio $(I_{LCP} - I_{RCP})/(I_{LCP} + I_{RCP})$ obtained with LCP and RCP incident x rays. The red curve is the fitting using the function of the order parameter in the second order transition [$\zeta(T) = \gamma(T_N - T)^\delta$ where $\gamma = 0.106$, $\delta = 0.627$, $T_N = 6.77$] and is a guide to the eye. (d) A photograph of sample 1. Two-dimensional maps of the flipping ratio of reflection 100 at (e) 298 K and (f) 6 K. The red-dashed box in (d) roughly represents the observation area.

color while the latter is red. This shows that in the map at room temperature [Fig. 3(e)] the magnitude of FR is negligibly small at the whole area, meaning that there is no significant circular dichroism. At 6 K ($<T_N$) [Fig. 3(f)], by contrast, substantial circular dichroism is present over the whole area of the sample. It is noted that the sign and the magnitude of FR are nearly independent of sample position (FR ≈ 0.06).

C. Formulation of cross section for resonant x-ray scattering

To clarify the origin of the observed circular dichroism at reflection 100 below T_N, we formulate the cross section for RXD of $Pb(TiO)Cu_4(PO_4)_4$. Following the derivation given in [12,21], we simplify Eq. (3) and obtain the scattering amplitude operator as

$$f = \begin{pmatrix} 0 & b\mathbf{F}_m \cdot \hat{\mathbf{q}} + A \\ -b\mathbf{F}_m \cdot \hat{\mathbf{q}}' + A & b\mathbf{F}_m \cdot (\hat{\mathbf{q}}' \times \hat{\mathbf{q}}) \end{pmatrix}, \tag{10}$$

where $b = -(\frac{3}{4\pi q})i(F^1_{-1} - F^1_{+1})$ and $A = \cos\theta(F_1 \sin\psi - iF_2 \cos\psi)$. f is represented by using the unit (**I**) and Pauli ($\boldsymbol{\sigma}$) matrices [12],

$$f = \mathbf{I}\beta + \boldsymbol{\alpha} \cdot \boldsymbol{\sigma} = \begin{pmatrix} \beta + \alpha_3 & \alpha_1 - i\alpha_2 \\ \alpha_1 + i\alpha_2 & \beta - \alpha_3 \end{pmatrix}, \tag{11}$$

where $\boldsymbol{\alpha}[= (\alpha_1, \alpha_2, \alpha_3)]$ and β are complex number coefficients. The expectation value of $f^\dagger f$ gives the formulated polarization-dependent cross section $d\sigma/d\Omega$ by taking the trace of $\boldsymbol{\mu} f^\dagger f$,

$$\frac{d\sigma}{d\Omega} = \boldsymbol{\alpha}^\dagger \cdot \boldsymbol{\alpha} + \beta^*\beta + \beta^*(\mathbf{P} \cdot \boldsymbol{\alpha}) + (\mathbf{P} \cdot \boldsymbol{\alpha}^\dagger)\beta + i\mathbf{P} \cdot (\boldsymbol{\alpha}^\dagger \times \boldsymbol{\alpha}). \tag{12}$$

Here, $\boldsymbol{\mu}$ is the density operator of the polarization state defined as $\boldsymbol{\mu} = \frac{1}{2}(\mathbf{I} + \mathbf{P} \cdot \boldsymbol{\sigma})$, where $\mathbf{P}$ [$= (P_1, P_2, P_3)$] is the Poincaré-Stokes parameters [30] representing the polarization states of x rays. The first and second terms in Eq. (12) are independent of the polarization state, while the others depend on the polarization state. Comparing Eqs. (10) and (11), the following relations are obtained:

$$2\beta = b\mathbf{F}_m \cdot (\hat{\mathbf{q}}' \times \hat{\mathbf{q}}),$$

$$2\alpha_1 = b\mathbf{F}_m \cdot (\hat{\mathbf{q}} - \widehat{\mathbf{q}'}) + 2A,$$
$$2\alpha_2 = ib\mathbf{F}_m \cdot (\hat{\mathbf{q}} + \widehat{\mathbf{q}'}),$$
$$2\alpha_3 = -b\mathbf{F}_m \cdot (\widehat{\mathbf{q}'} \times \hat{\mathbf{q}}). \quad (13)$$

Then, one can derive the respective terms in Eq. (12). From the first and the second terms, the polarization-independent cross section is

$$\frac{d\sigma}{d\Omega}_{\text{indep}} = \frac{|b|^2}{2}(|\mathbf{F}_m \cdot \hat{\mathbf{q}}|^2 + |\mathbf{F}_m \cdot (\widehat{\mathbf{q}'} \times \hat{\mathbf{q}})|^2 + |\mathbf{F}_m \cdot \widehat{\mathbf{q}'}|^2) + |A|^2 + \text{Re}[A^* b\mathbf{F}_m] \cdot (\hat{\mathbf{q}} - \widehat{\mathbf{q}'}). \quad (14)$$

When incident x rays are circularly polarized with $\mathbf{P} = (0,\ P_2,\ 0)$, the third, fourth, and fifth terms of Eq. (12) lead to the circular dichroic cross section:

$$\frac{d\sigma}{d\Omega}_{\text{circ}} = P_2|b|^2\text{Im}[\mathbf{F}_m \cdot (\widehat{\mathbf{q}'} \times \hat{\mathbf{q}})\mathbf{F}_m^* \cdot \widehat{\mathbf{q}'}] - P_2\text{Im}[A^* b\mathbf{F}_m \cdot (\widehat{\mathbf{q}'} \times \hat{\mathbf{q}})]. \quad (15)$$

In the present experimental setup where $\boldsymbol{\tau} = (1\ 0\ 0)$, Eqs. (14) and (15) give

$$\frac{d\sigma}{d\Omega}_{\text{indep}} = \frac{|b|^2}{2}[2|(iF_{mb}\cos\psi + F_{mc}\sin\psi)\cos\theta|^2 + |(F_{mc}\cos\psi - iF_{mb}\sin\psi)\sin 2\theta|^2] + |F_1\sin\psi\cos\theta - iF_2\cos\psi\cos\theta|^2, \quad (16)$$

$$\frac{d\sigma}{d\Omega}_{\text{circ}} = P_2|b|^2\cos\theta\sin 2\theta\text{Im}[(F_{mc}\cos\psi + iF_{mb}\sin\psi) \times (iF_{mb}\cos\psi - F_{mc}\sin\psi)] - P_2\cos\theta\sin 2\theta\ \text{Im}[(iF_2\cos\psi + F_1\sin\psi) \times b(F_{mc}\cos\psi - iF_{mb}\sin\psi)]. \quad (17)$$

At $\psi = 0^\circ$,

$$\frac{d\sigma}{d\Omega}_{\text{indep}} = F_2^2\cos^2\theta + \frac{|b|^2}{2}\left(2F_{mb}^2\cos^2\theta + F_{mc}^2\sin^2 2\theta\right), \quad (18)$$
$$\frac{d\sigma}{d\Omega}_{\text{circ}} = P_2\cos\theta\sin 2\theta\left(F_{mc}F_{mb}|b|^2 - F_{mc}F_2\text{Re}[b]\right). \quad (19)$$

The first term of Eq. (18) is the contribution of the ATS scattering, which is observed even above T_N. The second and third terms of Eq. (18) represent the contribution of the magnetic scattering and thus develop below T_N. The first term of Eq. (19) is a product of the two magnetic components F_{mc} and F_{mb} in Eq. (9) while the second one is that of F_{mc} and the component in the ATS scattering F_2. Thus, the circular polarization dependence of the scattering intensity is attributed to these interference effects. Note that $\frac{d\sigma}{d\Omega}_{\text{circ}}$ at $\psi = 180^\circ$ is the same as Eq. (19), meaning that FR at $\psi = 180^\circ$ is expected to be the same as that at $\psi = 0^\circ$. Experimental results are roughly consistent with this expectation [see the blue and the purple data in Fig. 5(e)].

TABLE I. Effects of the sign reversal of the chirality C and the magnetic quadrupole order Q on some components in form factors and those on the first and the second terms in Eq. (17). The asterisk (*) denotes the sign reversal of each component accompanied by that of C or Q.

Order parameter	F_2	F_{mb}	F_{mc}	First term in $\frac{d\sigma}{d\Omega}_{\text{circ}}$ ($\propto F_{mc}F_{mb}$)	Second term in $\frac{d\sigma}{d\Omega}_{\text{circ}}$ ($\propto F_{mc}F_2$)
C	*	*		*	*
Q		*	*		*

D. Effects of crystal chirality and magnetic quadrupole order on circular dichroism

Considering Eq. (17), we examine the effect of the crystal chirality and the magnetic quadrupole order on the circular dichroism of reflection 100. $Pb(TiO)Cu_4(PO_4)_4$ has a pair of enantiomorphic $C-$ and $C+$ structures [Fig. 1(b)] with its chirality. Both structures are transformed to each other by the mirror operation $m_{\perp[110]}$, which reverses the sign of F_2 : $F_2 = 4(T_{zx}\sin 2\pi x - T_{yz}\sin 2\pi y) \leftrightarrow F_2 = -4(T_{zx}\sin 2\pi x - T_{yz}\sin 2\pi y) = 4(T_{yz}\sin 2\pi y - T_{zx}\sin 2\pi x)$, with an exchange of the x and y coordinates. (Note that the tensor T_{ij} is symmetric upon permutation of indices.) Below T_N, $Pb(TiO)Cu_4(PO_4)_4$ undergoes an AFM order which involves a ferroic order of magnetic quadrupole moments (Fig. 1). Since the magnetic quadrupole order breaks the time-reversal symmetry, there is a pair of domains related by the time-reversal operation $1'$ [compare upper and lower panels of Fig. 1(b)]. This operation reverses the signs of F_{mb} and F_{mc} simultaneously. Furthermore, the mirror operation $m_{\perp[110]}$, which reverses crystal and magnetic chirality, reverses the sign of F_{mb} but not F_{mc}, keeping the same sign of the quadrupole order. Table I summarizes the sign reversal of the first and the second terms in Eq. (17) together with those of F_2, F_{mb}, and F_{mc} accompanied by the sign reversal of the chirality C and the magnetic quadrupole order Q. This table clearly indicates that the signs of both the crystal chirality and the magnetic quadrupole order reflect circular dichroic signals of reflection 100. Since both the first and the second terms of Eq. (17) are odd against the sign change of the chirality C, the sign of circular dichroic signals depends on the handedness of the crystal chirality. By contrast, only the second term in Eq. (17) is odd against the sign change of magnetic quadrupole order Q, which changes the magnitude of circular dichroic signals by switching the sign of Q. Thus, in principle, the crystal chirality and the magnetic quadrupole domains can be resolved by measuring circular dichroism of reflection 100 at the resonance condition.

E. Experimental results of chirality-dependent circular dichroism

To see the effect of the crystal chirality on circular dichroism, similar experiments as described in Sec. IV B were performed on a levorotatory ($C-$) crystal (sample 2). The result is shown in Fig. 4. Reflection 100 at $E_{\text{ph}} = 930$ eV and $\psi = 0^\circ$ was observed at temperatures both above and below T_N [Figs. 4(a) and 4(b)] as observed in a dextrorotatory ($C+$) crystal (sample 1). In addition, the circular dichroism develops below T_N [Fig. 4(b)], but with the opposite sign of the circular

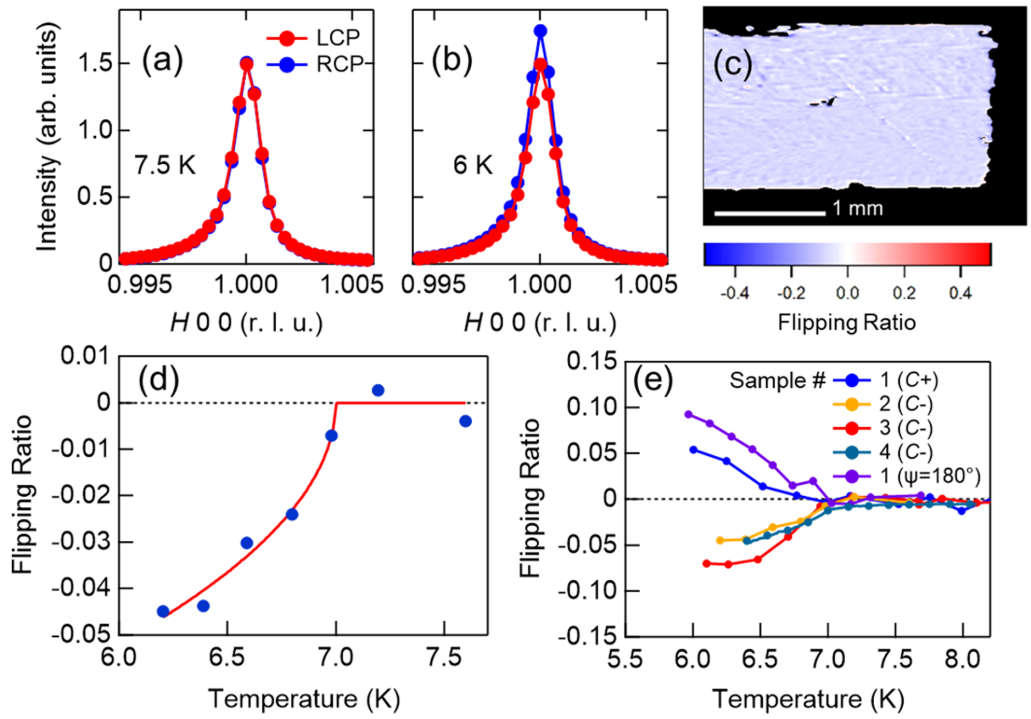

FIG. 4. Circular dichroism of resonant x-ray diffraction (RXD) of several samples. (a), (b) The H-scan profiles around 100 for a levorotatory ($C-$) crystal (sample 2). The data were taken at (a) 7.5 K and (b) 6 K using LCP and RCP incident x rays. (c) Two-dimensional map of the flipping ratio [FR $= (I_{\rm LCP} - I_{\rm RCP})/(I_{\rm LCP} + I_{\rm RCP})$]. The data were taken at $\psi = 0^\circ$ and 6 K. (d) Temperature dependence of FR obtained at reflection 100. The red curve is the fitting using the function of the order parameter in the second order transition [$\zeta(T) = \gamma(T_{\rm N} - T)^\delta$ where $\gamma = -0.0518$, $\delta = 0.503$, and $T_{\rm N} = 6.99$] and is a guide to the eye. (e) Temperature dependence of FR of reflection 100 in different samples (samples 1–4). For all the samples, the sign of FR below $T_{\rm N}$ corresponds with that of the crystallographic chirality. For sample 1 ($C+$ crystal), both the data at $\psi = 0^\circ$ and 180° show the positive sign of FR, which is consistent with Eq. (19).

dichroism. It is also evident by comparing Figs. 3(c) and 4(d). Below $T_{\rm N}$, FR in sample 1 is positive [Fig. 3(c)] while that in sample 2 is negative [Fig. 4(d)]. Furthermore, we measured a two-dimensional map of FR for reflection 100 of sample 2. Figure 4(c) displays the result and clearly shows nearly a uniform spatial distribution of FR, but the sign of FR is opposite to that in sample 1 [compare colors of the maps shown in Figs. 3(f) and 4(c)]. These results suggest that the crystallographic chirality reflects the circular dichroism. To further confirm the one-to-one correspondence between the sign of crystal chirality and that of circular dichroism, we performed the measurements on several crystals. The results are shown in Fig. 4(e) in which the sign of FR is closely correlated with the crystal chirality. This matches up nicely with the discussion given in Sec. IV D at which the sign of the circular dichroic cross section given in Eq. (17) is reversed by the sign change of the chirality (see Table I) in the case that the second term is smaller than the first term in Eq. (17). Thus the relation between crystal chirality C and F_{mb} provides the one-to-one correspondence. In other words, the crystal chirality which induces the chirality in magnetic structure contributes to circular dichroism of RXD at reflection 100.

F. Experimental results of circular dichroism ascribed to magnetic quadrupole order

Here we examine the effect of the magnetic quadruple order on the circular dichroism observed below $T_{\rm N}$. $Q+$ and $Q-$ domain states [upper and lower panels of Fig. 1(b)] are energetically degenerated in the absence of B and E. Therefore, these two states will coexist below $T_{\rm N}$ when the sample is cooled from the paramagnetic state in the absence of B and E, meaning that the experiments in the previous sections have been done in the multidomain state with both $Q+$ and $Q-$ domains. Such a state is not ideal to examine the contribution of the magnetic quadrupole order. In $Pb(TiO)Cu_4(PO_4)_4$ showing a linear ME effect [5], a monodomain state of $Q+$ or $Q-$ is achieved by the simultaneous application of a poling electric field ($E_{\rm pole}$) and a poling magnetic field ($B_{\rm pole}$) during cooling from the paramagnetic phase to the AFM phase (ME cooling) [8]. Therefore, we carried out RXD measurements after poling in both $E_{\rm pole}$ and $B_{\rm pole}$ applied along the [010] direction. This ME-cooling procedure stabilizes a monodomain state, which has been confirmed by a previous ME measurement on $Pb(TiO)Cu_4(PO_4)_4$ [5].

Figure 5(a) shows the effect of $E_{\rm pole}$ and $B_{\rm pole}$ on the temperature dependence of the reflection intensity at 100 observed at $E_{\rm ph} = 930$ eV and $\psi = 0^\circ$ for a levorotatory ($C-$) crystal (sample 4). In this measurement, $B_{\rm pole}(\|[010])$ was fixed at about 0.1 T and an unfocused x-ray beam with the irradiation area of approximately 1 mm × 1 mm was used. It is expected that this unfocused x-ray beam provides an averaged signal from a multidomain state of $Q+$ and $Q-$ to some extent. For the data of $E_{\rm pole} = 0$ (zero-field cooling) [green lines in Fig. 5(a)], substantial circular dichroism with $(I_{\rm LCP} - I_{\rm RCP}) < 0$ is observed, which is qualitatively consistent with the result of other $C-$ crystals [see Fig. 4(e)].

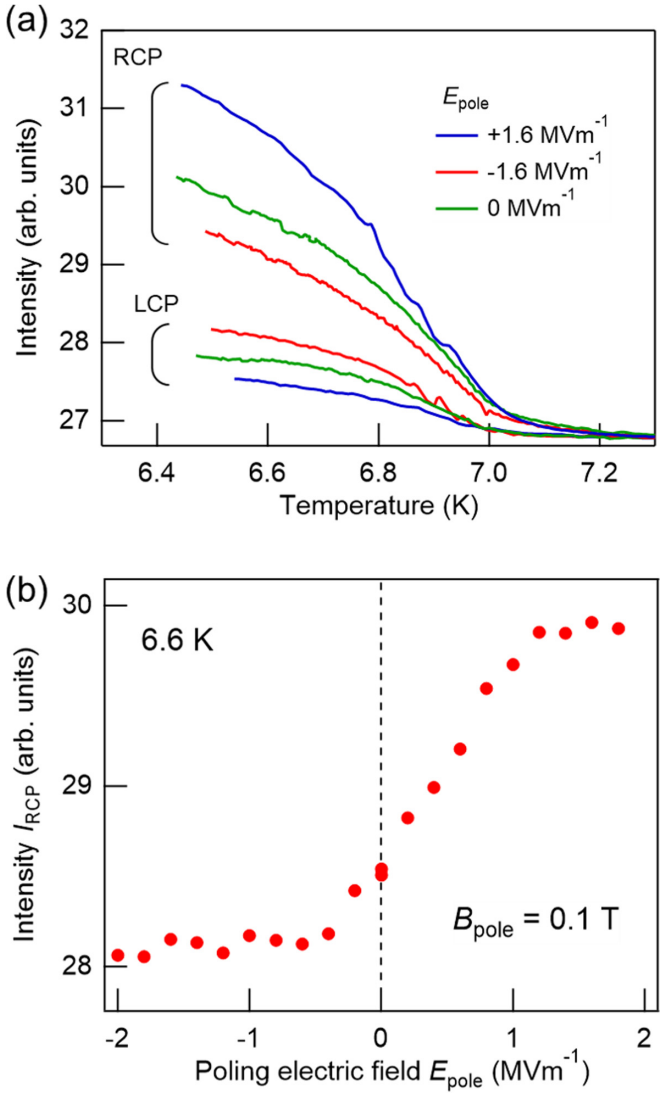

FIG. 5. Magnetoelectric-cooling effect on circular dichroism below T_N at $\psi = 0°$ observed in sample 4. (a) Temperature dependence of the diffracted intensity of reflection 100 with different poling electric fields (E_{pole}) along the [010] direction. The poling magnetic field along [010] was fixed at 0.1 T in all the measurements. (b) E_{pole} dependence of the diffracted intensity at 6.6 K. The data obtained with RCP x rays are adopted.

As seen in Fig. 5(a), the ME cooling explicitly affects the reflection intensity. In the data of $E_{pole} = +1.6\,\mathrm{MV\,m^{-1}}$, I_{RCP} increases while I_{LCP} decreases. By contrast, in the data of $E_{pole} = -1.6\,\mathrm{MV\,m^{-1}}$, I_{RCP} decreases while I_{LCP} increases. Thus, the circular dichroic signal is enhanced (suppressed) by applying a positive (negative) poling electric field. Figure 5(b) shows I_{RCP} at 6.6 K as a function of E_{pole}. I_{RCP} depends linearly on E_{pole} in the range of $-0.4\,\mathrm{MV\,m^{-1}} < E_{pole} < +1.2\,\mathrm{MV\,m^{-1}}$. However, it becomes nearly saturated at $E_{pole} < -0.4\,\mathrm{MV\,m^{-1}}$ and $E_{pole} > +1.2\,\mathrm{MV\,m^{-1}}$. This feature suggests that either $Q+$ or $Q-$ monodomain state is achieved in these E_{pole} regions. The observed ME cooling effect on circular dichroism is well explained by the second term in Eq. (17), which is smaller than the first term, and ascribed to the change of domain population of the magnetic quadrupole order. This result clearly shows that we can probe the order parameter of magnetic quadrupole order qualitatively by measuring circularly polarized RXD through the interference between the ATS and the magnetic scatterings. Note that the data shown in Fig. 5(b) is not symmetric with respect to E_{pole} (bias field $\approx +0.5\,\mathrm{MV\,m^{-1}}$) though the fraction of $Q+$ and $Q-$ domains is ideally equal with each other when a sample is zero-field cooled. We consider that the observed bias effect could be related to a memory effect of the domain structure previously reported in $Pb(TiO)Cu_4(PO_4)_4$ [8] whose domains are likely pinned by defects formed during crystal growth or other reasons such as local thermal inhomogeneity created in the sample.

V. SUMMARY

In summary, we demonstrate that the circularly polarized resonant x-ray diffraction at the Cu L_3 edge enables us to examine both crystal chirality and magnetic quadrupole order in a chiral antiferromagnet $Pb(TiO)Cu_4(PO_4)_4$. Circular dichroism on the diffraction intensity of a forbidden reflection was observed in the ordered phase. We found that the sign of the circular dichroic signal in a levorotatory crystal is opposite to that of a dextrorotatory crystal. This circular dichroism is ascribed to the magnetic chirality induced by the crystallographic chirality in this compound. Besides, the magnitude of the circular dichroic signal systematically changes with varying fraction of the magnetic quadrupole domains, which was demonstrated by measuring after magnetoelectric cooling. The observed circular dichroism on the resonant x-ray diffraction is interpreted as the interference between the ATS and the magnetic scatterings, which allows for probing both the magnetic chirality dominated by the crystallographic one and the order parameter of the magnetic quadrupole order. The present study proves the effectiveness of resonant x-ray diffraction for the investigation of chiral magnetism embedded on the crystallographic chirality as well as parity- and time-odd multipoles. Furthermore, we show that the crystallographic chirality contributes to magnetic and ME phenomena in systems with ferroic order of such multipoles.

ACKNOWLEDGMENTS

We thank T. Katsuyoshi for help with experiments and J. K. H. Fischer for English language editing. This work was supported by a Grant-in-Aid for JSPS Fellows (Grant No. JP19H00661) and KAKENHI (Grants No. JP17H01143, No. JP19J00467, No. JP19H01847, and No. JP19H05823). Soft x-ray experiments were performed at the beamline 17SU at SPring-8 with the approval from RIKEN (Proposals No. 20180021, No. 20190004, and No. 20200012). H.U. acknowledges financial support by the National Centers of Competence in Research in Molecular Ultrafast Science and Technology (NCCR MUST-No. 51NF40-183615) from the Swiss National Science Foundation and from Horizon 2020, the EU Framework Programme for Research and Innovation under Marie Skłodowska-Curie Grant Agreement No. 801459-FP-RESOMUS.

[1] D. I. Khomskii, *Transition Metal Compounds* (Cambridge University Press, Cambridge, UK, 2014).
[2] Y. Kuramoto, Prog. Theor. Phys. Suppl. **176**, 77 (2008).
[3] N. A. Spaldin, M. Fechner, E. Bousquet, A. Balatsky, and L. Nordstrom, Phys. Rev. B **88**, 094429 (2013).
[4] Y. Yanase, J. Phys. Soc. Jpn. **83**, 014703 (2014).
[5] K. Kimura, M. Toyoda, P. Babkevich, K. Yamauchi, M. Sera, V. Nassif, H. M. Rønnow, and T. Kimura, Phys. Rev. B **97**, 134418 (2018).
[6] H. Watanabe and Y. Yanase, Phys. Rev. B **98**, 245129 (2018).
[7] Y. Shiomi, H. Watanabe, H. Masuda, H. Takahashi, Y. Yanase, and S. Ishiwata, Phys. Rev. Lett. **122**, 127207 (2019).
[8] K. Kimura, T. Katsuyoshi, Y. Sawada, S. Kimura, and T. Kimura, Commun. Mater. **1**, 39 (2020).
[9] K. Kimura, Y. Kato, S. Kimura, Y. Motome, and T. Kimura, (unpublished).
[10] J. Hlinka, Phys. Rev. Lett. **113**, 165502 (2014).
[11] S.-W. Cheong, S. Lin, K. Du, and F.-T. Huang, arXiv:2101.03123.
[12] S. W. Lovesey and S. P. Collins, *X-ray Scattering and Absorption by Magnetic Materials* (Oxford Science Publications, Clarendon, Oxford, 1996).
[13] S. P. Collins, S. W. Lovesey, and E Balcar, J. Phys.: Condens. Matter **19**, 213201 (2007).
[14] J. Fink, E. Schierle, E. Weschke, and J Geck, Rep. Prog. Phys. **76**, 056502 (2013).
[15] Y. Tanaka, T. Inami, S. W. Lovesey, K. S. Knight, F. Yakhou, D. Mannix, J. Kokubun, M. Kanazawa, K. Ishida, S. Nanao, T. Nakamura, H. Yamauchi, H. Onodera, K. Ohoyama, and Y. Yamaguchi, Phys. Rev. B **69**, 024417 (2004).
[16] D. Mannix, Y. Tanaka, D. Carbone, N. Bernhoeft, and S. Kunii, Phys. Rev. Lett. **95**, 117206 (2005).
[17] S. Di Matteo, J. Phys. D: Appl. Phys. **45**, 163001 (2012).
[18] S. W. Lovesey and G. van der Laan, Phys. Rev. B **98**, 155410 (2018).
[19] S. L. Zhang, G. van der Laan, and T. Hesjedal, Phys. Rev. B **96**, 094401 (2017).
[20] S. Tardif, S. Takeshita, H. Ohsumi, J.-I. Yamaura, D. Okuyama, Z. Hiroi, M. Takata, and T.-H. Arima, Phys. Rev. Lett. **114**, 147205 (2015).
[21] H. Ueda, Y. Tanaka, Y. Wakabayashi, and T. Kimura, Phys. Rev. B **98**, 134415 (2018).
[22] Y. Tanaka, T. Takeuchi, S. W. Lovesey, K. S. Knight, A. Chainani, Y. Takata, M. Oura, Y. Senba, H. Ohashi, and S. Shin, Phys. Rev. Lett. **100**, 145502 (2008); **108**, 019901(E) (2012).
[23] T. Usui, Y. Tanaka, H. Nakajima, M. Taguchi, A. Chainani, M. Oura, S. Shin, N. Katayama, H. Sawa, Y. Wakabayashi, and T. Kimura, Nat. Mater. **13**, 611 (2014).
[24] T. Takeuchi, A. Chainani, Y. Takata, Y. Tanaka, M. Oura, M. Tsubota, Y. Senba, H. Ohashi, T. Mochiku, K. Hirata, and S. Shin, Rev. Sci. Instrum. **80**, 023905 (2009).
[25] L. D. Landau and E. M. Lifshitz, *Quantum Electrodynamics*, 2nd ed., Vol. 4 (Pergamon, Oxford, 1982).
[26] D. H. Templeton and L. K. Templeton, Acta Crystallogr., Sect. A **41**, 133 (1985); **42**, 478 (1986).
[27] V. E. Dmitrienko, Acta Crystallogr., Sect. A **39**, 29 (1983).
[28] Y. Joly, Phys. Rev. B **63**, 125120 (2001).
[29] O. Bunau and Y. Joly, J. Phys.: Condens. Matter **21**, 345501 (2009).
[30] C. Detlefs, Eur. Phys. J.: Spec. Top. **208**, 359 (2012).